Journal of Industrial and Engineering Chemistry xxx (xxxx) 1–13

Contents lists available at ScienceDirect

Journal of Industrial and Engineering Chemistry

journal homepage: www.elsevier.com

Full Length Article

"O-S" charge transfer mechanism on electron-extracting system: Interface engineered Ag-r-GO-$CuFe_2O_4$-Fe_3O_4 heterojunction an efficient photocatalyst for water treatment and toxicity study in *Trifolium* plants

Balasurya Senthilmurugan [a, b], Mohammad K. Okla [c], Mostafa A. Abdel-Maksoud [c], Saud S Al-Amri [c], Ibrahim A. Alaraidh [c], Abdulrahman A. Alatar [c], Abdelrahim H. A. Hassan [d, e], Mohamed S. Sheteiwy [f, g], Hamada AbdElgawad [h], S. Sudheer Khan [i, *]

[a] *Nanobiotechnology Laboratory, Department of Biotechnology, Bannari Amman Institute of Technology, Sathyamangalam, Tamil Nadu, India*
[b] *Centre Énergie, Matériaux et Télécommunications, INRS, Varennes, Québec J3X1S2, Canada*
[c] *Botany and Microbiology Department, College of Science, King Saud University, P.O. Box 2455, Riyadh 11451, Saudi Arabia*
[d] *School of Biotechnology, Nile University, Giza 12588, Egypt*
[e] *Department of Food Safety and Technology, Faculty of Veterinary Medicine, Beni-Suef University, Beni-Suef, Egypt*
[f] *Department of Integrative Agriculture, College of Agriculture and Veterinary Medicine, United Arab, Emirates University, Al-Ain, Abu-Dhabi, UAE*
[g] *Department of Agronomy, Faculty of Agriculture, Mansoura University, Mansoura, Egypt*
[h] *Integrated Molecular Plant Physiology Research, Department of Biology, University of Antwerp, Antwerp, Belgium*
[i] *Department of Oral Medicine and Radiology, Saveetha Dental College and Hospitals, Saveetha Institute of Medical and Technical Sciences (SIMATS), Chennai 600077, Tamil Nadu, India*

ARTICLE INFO

Article history:
Received 9 August 2023
Received in revised form 12 January 2024
Accepted 18 January 2024

Keywords:
O-S mechanism
Ag-r-GO-$CuFe_2O_4$-Fe_3O_4 NCs
Industrial effluent
Photocatalysis

ABSTRACT

Herein, we report the Ohmic and Schottky junction (O-S scheme) Ag-r-GO-$CuFe_2O_4$-Fe_3O_4 nanocomposite (Ag-r-GO-CFO-FO NCs) for effective photocatalytic activity against organic pollutants. Herein the O-S scheme mechanism is achieved by the formation of Ohmic and Schottky junctions. The two interfacial charge carriers for accelerated phono formation and mass transfer and thus increase in the light-harvesting with electron traps for the gerenation of reactive oxygen species (ROS). The photocatalytic activity of the constructed Ag-r-GO-CFO-FO NCs was tested against organic dyes (red RB, orange 2R and black B) and the degradation efficiency was calculated to be 99.8, 99.3 and 99.8% respectively. The radical quenching shows the formation of •OH and O_2•- which plays major role in the mineralization of organic pollutants. Total organic carbon (TOC) after the degradation of red RB, orange 2R and black B by Ag-r-GO-CFO-FO NCs was 2.1%, 1.6% and 1.9% respectively, which shows the complete mineralization of the pollutants. In addition, the real-time application of the photocatalytic efficiency of NCs was performed against the effluent collected from dying industrial (which is a combination of red RB, orange 2R and black B) and the degradation efficiency was 98.2%. Toxicity of the NCs was performed against maize plants, the results show that the NCs are non-toxicity towards plants and can be used for real-time application. The efforts provide evidence of the combination of two interfacial charge carriers (O-S scheme) to boost the catalytic activity of the catalyst for water treatment.

Introduction

In the past few decades, environmental water contamination significantly increased on modernization and industrialization which has deteriorated effect on environmental water bodies [1–4]. Freshwater contamination is one the major crises in the world and the contamination are categorized into industrial and municipal contaminants. The direct discharge of non-treated wastewater causes hazardous effects to the eco-system because of the stable and toxic organic pollutants like dye, antibiotics, dissolved salts etc [5–7]. Several methods were employed for the effective water treatment such as photolysis (with UV and H_2O_2), osmosis, adsorption, active carbon, ozonation, advanced oxidation process and photocatalysis. Among the available methods, photocatalysis is one of the most effective methods for the removal of organic contaminants by using solar energy [8–12]. An ideal photocatalytic process is to harvest the solar energy and rapidly produce e^-/h^+ pair for the timely surface redox reaction on the mineralization of the pollutant [13–16]. On the other hand, the realization of an effective photocatalyst has a major concern on the efficiency of mineralization of contaminants. The recent invention in the coupling effect of catalyst on the for-

* Corresponding author.
E-mail address: sudheerkhans.sdc@saveetha.com (S. Sudheer Khan).

https://doi.org/10.1016/j.jiec.2024.01.046
1226-086/© 20XX

mation of heterojunction enhances the photocatalytic activity, which indeed on the formation of type I, II and Z-scheme heterojunction [17–21]. Nevertheless, the formation of nano-heterojunction to improve the catalytic activity of NCs is still not reached a satisfactory degree. It is indeed to develop a tool for the effective mineralization of organic pollutants.

Ferrate-based semiconductor $CuFe_2O_4$ (CFO) has been widely used for the photocatalytic reduction of organic compounds, owing to its narrow band gap in the range of 1.5 to 1.95 eV, where the positive conduction band potential fails in the photoconversion of oxygen [22]. However, the coupling of CFO with Fe_3O_4 (FO) enables the effective photoreduction and photo-oxidation between photosystem I and photosystem II. The Fe_3O_4 semiconductor with higher negative conduction bands enhances the effective charge transfer. Over pristine photosystem, the sluggish photocarrier separation is still not desired to a satisfactory degree [23,24]. Graphite-based material has been extensively used as a photovoltaic and photocatalytic due to its extensive electronic structure [24]. A quadrant nano-heterojunction on the coupling of r-GO and Ag was employed to increase the charge separation and the electronic transfer between the photosystems [24,25]. Silver-based nanomaterial is widely used in several applications due to its extensive surface plasmon resonance properties [26]. The 2D sheet of Ag and r-GO act as an electron trap which enhances the photoexcitation and thereby increases the catalytic activity of NCs [24,27–29]. Here, the coupling of the high positive potential conduction band (CFO) with the high negative potential valance band (FO) intent on the formation of an interfacial Schottky barrier (Schottky-like junction) to facilitate the charge transfer between the photosystems [30]. Meanwhile, the coupling of Ag-r-GO with the Schottky-like junction forms an ohmic contact between the heterojunction (Ohmic like junction). Ohmic junction acts as an electron trap and pumps the electron from Ag-r-GO to the Schottky junction (CFO-FO) which facilitates the effective photo-oxidation and photo-reduction of O_2 and OH^-.

TiO_2 is an evident, promising, and standard photocatalyst which is been already marketed as the standard nanomaterial for catalysis [31, 32]. Nevertheless, it has its own disadvantages like wide band gap and mass transfer, whereas it is essential to develop a different nanomaterial system to overcome shortcomings. Herein, a quadrant nanoheterojunction Ag-r-GO-CFO-FO NCs on the formation of Ohmic-Schottky junction was constructed by sono-chemical method, which enables the lattice oxygen defect and point defect. The photocatalytic activity of novel O-S charge transfers a nanoheterojunction was studied against the standard dyeing organic chemical. Further, the photocatalytic activity was tested against the effluent collected from a dying industry. Besides the lattice mismatch on the formation of quadrant nanoheterojunction on the Ohmic-Schottky junction, O-S charge transfer mechanism on the nanoheterojunction provides the facile and newfangled strategy for the environmental water treatment.

Experiment

Synthesis of Ag-rGO-$CuFe_2O_4$-Fe_3O_4

Synthesis of r-GO-$CuFe_2O_4$

The r-GO nanosheets were prepared via the Hummers method [30]. Here, $CuFe_2O_4$ nano-spines were fabricated by chemical co-precipitation followed by reflux [33]. Briefly, 0.4 g of r-GO was added to a solution contains 30 mL of $CuSO_4$ (0.1 M), and 30 mL of $FeSO_4$ (0.2 M), and dispersed under ultrasonication for 20 min. Then, 5 mL of NaF (0.2 M) and 30 mL of urea (0.2 M) were added to the above mixture and kept in a stirrer for 20 min to obtain a homogenous mixture. Then, the solution was transferred to the double necked round bottom flask and kept at 110 °C for 18 h. The prepared nanomaterial was collected by centrifugation, washed twice with ethanol and water, dried at 80 °C for 60 min. Then the prepared nanomaterial was calcinated at 500 °C for 5 h. The pure $CuFe_2O_4$ was fabricated in absence of r-GO.

Synthesis of r-GO-$CuFe_2O_4$-Fe_3O_4

r-GO-$CuFe_2O_4$-Fe_3O_4 (r-GO-CFO-FO) nanomaterial was fabricated by sono-chemical method [34]. Firstly, 0.192 g of r-GO-CFO was dispersed in 100 mL for 20 min with ultrasonic pulse rate of 30 sec (on): 10 sec (off). Then, 8 mM of $FeSO_4$ was added to the above mixture and stirred for 20 min to obtain a homogenous solution. Thereafter, 100 mL of NaOH (0.1 M) was injected to the above mixture under ultrasonication with 3 sec (on): 1 sec (off) pulse. The formed nanomaterial was collected by centrifugation, washed twice with water and ethanol, dried at 80 °C for 80 min and named r-GO-CFO-FO-30. Similarly, 4 mM and 6 mM of $FeSO_4$ were used for the fabrication of r-GO-CFO-FO-10, and r-GO-CFO-FO-20 respectively, and the pure Fe_3O_4 nanoparticles (FO NPs) was fabricated in the absence of r-GO-CFO.

Synthesis of Ag-rGO-$CuFe_2O_4$-Fe_3O_4 NCs

Ag decorated rGO-$CuFe_2O_4$-Fe_3O_4 nanocomposite (Ag-r-GO-CFO-FO NCs) was fabricated by a simple chemical reduction method [35]. Here, the fabricated rGO-$CuFe_2O_4$-Fe_3O_4 was dispersed for 15 min in 50 mL of $AgNO_3$ (5 mM) (Solution A). Then, 50 mL of ice-chilled $NaBH_4$ was prepared and added dropwise to the above solution and stirred for 20 min. The prepared nanomaterial was centrifuged at 10000 rpm and washed twice with ethanol and water. Here, the prepared NCs were dried at 80 °C for 60 min and named Ag-r-GO-CFO-FO-5. Similarly, 3 mM and 1 mM $AgNO_3$ were used for the fabrication of Ag-r-GO-CFO-FO-3 and Ag-r-GO-CFO-FO-1 respectively.

Photocatalytic experiment

The photocatalytic activity of Ag-r-GO-CFO-FO, r-GO, CFO and FO nanomaterial was performed against Red RB, Orange 2R and Black B under the irradiation of 1000 W Halogen lamp with a working distance of 15 cm (difference in the height between light and reaction mixture),1 where UV filter was used for the visible light irradiation [36, 37]. Briefly, NCs (20 mg/L) were added to the 20 mL of organic dye (100 mg/L) at pH 7 and the reaction mixture was stirred for 30 min to obtain the adsorption equilibrium. Then, the reaction mixture was irradiated under visible light and the UV–visible absorption spectroscopy was recorded in the range of 200 to 700 nm until the complete degradation of the organic dye. Similarly, the similar experiment was performed with pH (5 to 9), NCs dosage (5 to 25 mg/L) and dye concentration (25 to 150 mg/L). The real-time application on the photocatalytic activity of the NCs was determined by using industrial dye effluent collected from Sivasakthi Tex, Tirupur, Tamil Nadu, India and the degradation efficiency was calculated.

Experimental setup greenhouse pot experiment

Seeds of *Trifolium repens* with healthy condition were cultivated in pots (25 cm × 30 cm) filled with sterilized clay soil. The selection of chemical dosage was based on a preliminary study encompassing various concentrations (0–500 mg/L). The plants were subjected to treatment with two dosages (10 and 100 mg/L) of each nanomaterial (r-GO, CFO_3, FO, and Ag-r-GO-CFO-FO NCs). Cultivation occurred in a controlled environment within a growth room (21/18 °C, 16/8h day/night cycle, 220 mM PAR 1/m²s, and 62 % humidity). The soil received watering twice daily. Assessment of *Trifolium* shoot biomass took place after 6 weeks of growth, and the harvested samples were stored at −80 °C for subsequent investigations.

Determination of photosynthesis

The infrared gas analyzer (PP Systems, Hitchin, UK) was utilized to determine the photosynthesis as μM CO_2 m^2/s of treated and untreated groups. The photosynthesis rates of Trifolium plants were calculated from about 3.5 min of net exchange of CO_2 measurements [38].

Determination of mineral contents

For the assessment of macro and micro element content, *Trifolium* plant samples of each 200 mg underwent acidic digestion in a HNO_3/H_2O solution (5:1 v/v) within an oven. The concentrations of macro and trace elements were determined at 25 ˚C using inductively coupled plasma mass spectrometry (Finnigan Element XR Scientific, Germany). HNO_3 at 1 % served as the standard [39].

Determination of total antioxidant capacity and antioxidant metabolites

The in vitro assessment of antioxidant capacity utilized the ferric reducing antioxidant power (FRAP) method [40]. *Trifolium* sample of approx. 0.2 g was extracted with ethanol (80 %). Centrifugation of samples were run for 20 min at 14,000 rpm. The antioxidant capacity was determined by combining diluted extract (0.1 mL) with FRAP reagent (0.25 mL, a mixture of $FeCl_3$ (20 mM) in acetate buffer (pH 3.6, 0.25 M)) at room temperature [41]. The absorbance at 517 nm was recorded using a spectrophotometer. Flavonoids and polyphenols were quantified by homogenizing freeze-dried plants (100 mg) in ethanol (80 % v/v). Samples were centrifuged at 4 ˚C for 20 min and the supernatant was employed to determine total flavonoid and phenolic contents. The Folin–Ciocalteu assay with gallic acid as a standard was deployed for phenolic content determination, while the modified aluminum chloride colorimetric method with quercetin as a standard was applied for flavonoid content determination [42,43].

Determination of primary metabolites

Lemongrass sprouts or seeds (100 mg) were homogenized in aqueous ethanol (1 mL, 80 % v/v) to extract amino acids, with norvaline serving as an internal standard. A Waters Acquity UPLC TQD device, coupled to a BEH amide column, was utilized for amino acid estimation. The amino acid determination involved using the supernatant obtained after centrifugation (10 min, 8000 g) with 0.2 μm Millipore microfilters. For the analysis of organic acid levels, HPLC (C18 column; Shimadzu SIL10-ADvp, 4.6 × 250 mm, 5 μm particle diameter, Spherisorb ODS2, Waters) was employed following the method outlined by Shabbaj et al. (2021) [44]. In the determination of fatty acids, LN-fine powdered plant leaves (0.5 g) were extracted in aqueous methanol at 27 ˚C. The subsequent GC/MS analysis (Hewlett Packard 6890, MSD 5975 mass spectrometer, United States) was performed using an HP-5 MS column (30 m × 0.25 mm × 0.25 mm), and quantification of fatty acids was carried out using analyte/internal standard ion yield ratios [45].

Results and discussion

Characterization

Structural morphology

The morphological characteristic of the nanomaterial was determined by transmission electron microscopy (TEM) and scanning electron microscopy (SEM) analysis (Figs. 1 & 2). As shown in Fig. 2a & b, SEM image of CFO NPs implies the formation of nano-spines where rods were arranged in an array to form spines and SEM image of Fe_3O_4 shows the formation of irregularly shaped Fe_3O_4 with an average particle size of 26 nm. Here, the SEM image of the composite implies the formation of the cubic shape particles where 2D r-GO nanosheet acts as a base sheet for the formation of cubic NCs (Fig. 2c). Elemental mapping of Ag-r-GO-CFO-FO NCs shows the presence of Fe, Cu, O, C and Ag, which further confirms the formation of Ag-R-GO-CFO-FO NCs (Fig. 2d). TEM image of Ag-r-GO-CFO-FO NCs confirms the formation of cubic particles (Fig. 1a). The formation of nano heterojunction by r-GO, CFO, FO and Ag NPs can be clearly seen in TEM image (Fig. 1b). Selective area electron diffraction was performed to determine the crystallinity of the nanomaterial and the prepared Ag-r-GO-CFO-FO NCs implies the formation of cubic phase nano heterojunction. Fig. 1d shows the D spacing image of Ag-r-GO-CFO-FO NCs, where 0.12, 0.39 and 0.14 nm correspond to FO (4 0 0), CFO (2 2 0) and Ag (1 1 1) respectively.

XRD

The structural and crystalline properties of r-GO, CFO, FO and Ag-r-GO-CFO-FO NCs were determined by XRD analysis (Fig. 3a). XRD spectrum of CFO showed peaks with corresponding facets at 30.3˚ (2 0 0), 36˚ (2 1 1), 37.3˚ (2 0 2), 44˚ (2 2 0), 57.6˚ (3 2 1) and 62.8˚ (2 2 4) which corresponds to JCPDS card no: 00–034-0425. Here, the XRD peak 2θ at 30.1˚ (2 2 0), 35.4˚ (3 1 1), 37.1˚ (2 2 2), 43.2˚ (4 4 0), 53.6˚ (4 2 2), 57.1˚ (5 1 1), 62.8˚ (4 4 0) and 71.3˚ (6 2 0) corresponds to the FO (JCPDS card no: 00–065-0731). The XRD pattern of Ag-r-GO-CFO-FO NCs showed higher peak intensity and sifts at 35.5˚ and 39˚ ensuring the phase retention after the formation of nano-heterojunction. The observed peak shift indicates the un-similarity of the pure CFO, FO and Ag NPs. Besides the exhibition of CFO, FO and Ag NPs in NCs, the faint diffraction peak of NCs at 24˚ indicates the formation of r-GO nanosheets of (0 2 2) plane. The average crystalline size of the nanomaterial was determined by Equ. 1 [46].

$$D = \frac{0.9\,\lambda}{\beta\, cos\theta} \tag{1}$$

D represents the crystalline size, λ represents wavelength (λ = 1.54 Å) and β represents the peak broadening at FWHM. The crystalline size of the CFO, FO and Ag-r-GO-CFO-FO NCs was calculated to be 25.3 nm, 22.1 nm and 86.3 nm respectively. The increase in the size of the nanomaterial was due to the formation of heterojunction, where the decoration of Ag on r-GO-CFO-FO causes the change in the grain size of the NCs [47]. In addition, the particle size of the NCs was determined by the Williamson-Hall formula [48]. According to WH formula, the particle size of the CFO, FO and Ag-r-GO-CFO-FO NCs was calculated to be 25.9, 21.9 and 85.9 nm respectively. Here, the difference in the particle between Scherrer and Williamson-Hall was negligible thus indicating no strain. The dislocation density of the nanomaterial was determined by Euq. 2.

$$\delta = \frac{1}{D^2} \tag{2}$$

D represents the crystalline size and δ represents the dislocation density. Here, the density of dislocation of CFO, FO and Ag-r-GO-CFO-FO NCs was calculated to be 40.2 $lin.m^{-2}$, 38.6 $lin.m^{-2}$ and 29.2 $lin.m^{-2}$ respectively. The decrease in the dislocation density of NCs than the pure nanoparticle was due to the higher in crystalline size [47]. Porosity plays a major role in the photocatalytic degradation of organic pollutants. The higher photocatalytic activity of NCs on the pollutant removal was observed with the material of higher porosity. The porosity % of the nanomaterial was determined by Equ. 3 [47,49].

$$\%\,P = (1 - \frac{D_b}{D_x}) \tag{3}$$

In Equ. 3, D_b and D_x represent the bulk density and X-ray density respectively. The estimated porosity of CFO, FO and Ag-r-GO-CFO-FO NCs was 15.3, 16.2 and 22.4 % respectively.

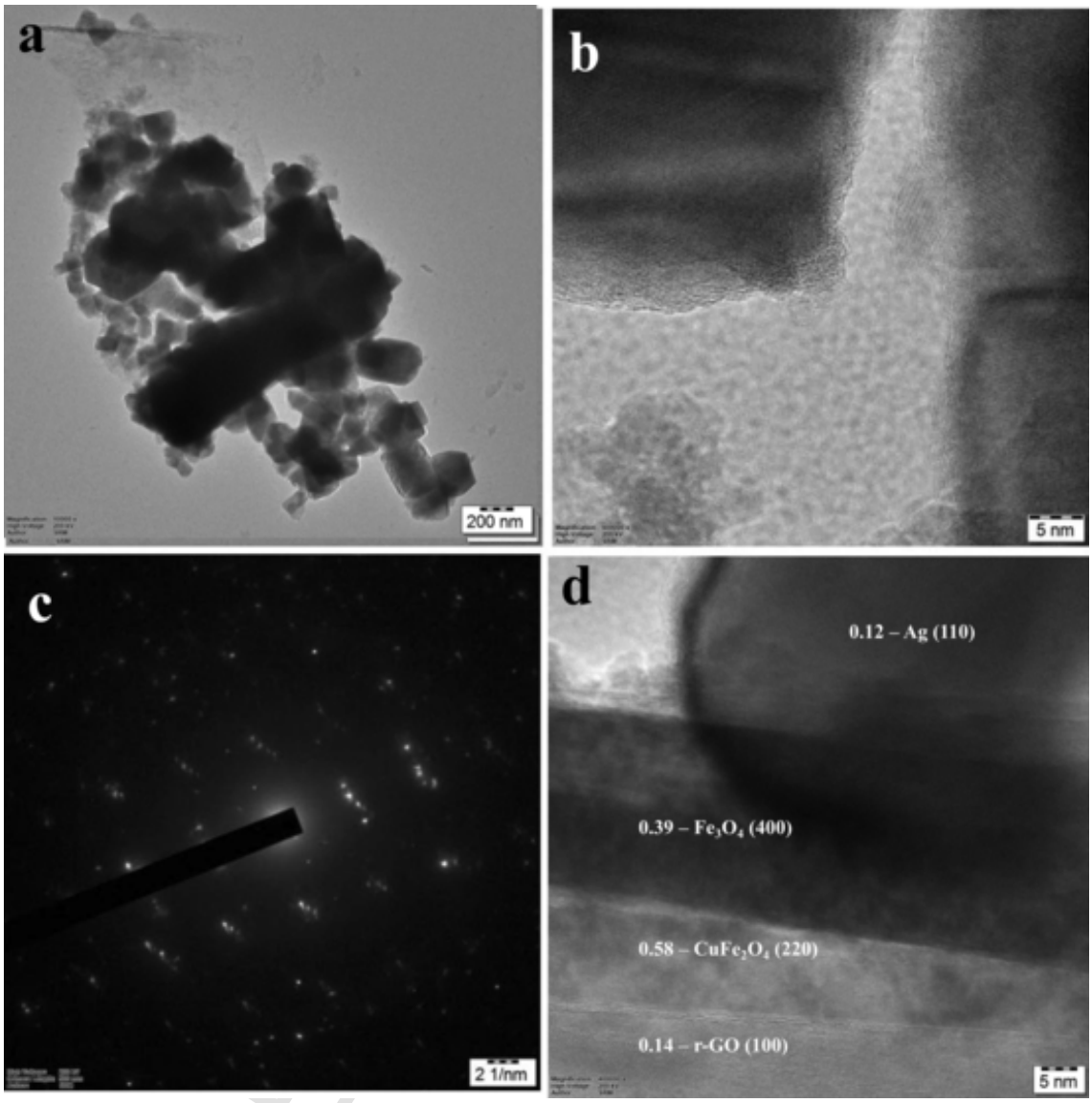

Fig. 1. TEM image (a, b), SAED (c) and d-spacing (d) of Ag-r-GO-CFO-FO NCs.

Raman analysis

The point defect on the nanomaterial was further determined by the Raman spectroscopy (Fig. 3b). Here, the spectrum at 683, 617, 563 and 471 cm^{-1} correspond to the tetrahedral plane of the CFO nanomaterial [50]. The higher peak intensity at 969 cm^{-1} indicates the Ag decoration for the formation of NCs [50]. The peak at 274, 388 and 585 cm^{-1} represent the crystalline phase of Fe_3O_4 nanoparticle [51]. The Raman peaks at 1350, 1600 and ~2885 cm^{-1} corresponds to G, D and 2D band. The defect density of Ag-r-GO-CFO-FO NCs was determined by Equ. 4.

$$n_D(cm^{-1}) = 7.3 \times 10^9 E_L^4 \left(\frac{I_D}{I_G}\right) \quad (4)$$

The defect density of Ag-r-GO-CFO-FO NCs was calculated to be 8.4 x 10^{10} cm^{-1} and the defect density of CFO, and FO was 6.2 x 10^{10} cm^{-1} and 2.3 x 10^{10} cm^{-1} respectively.

BET

BET adsorption and desorption isotherm of the CFO, FO and Ag-r-GO-CFO-FO NCs follows Type IV isotherm with H3 loop (Supplementary material Fig. S1a and b) [52]. Here, the surface area, pore-size and pore-radius of CFO were 44.63 m^3/g, 0.072 cc/g and 2.042 nm respectively, and for FO it was 94.94 m^3/g, 0.161 cc/g and 1.48 nm respectively. The surface area, pore size and pore radius of Ag-r-GO-CFO-FO NCs was 100.78 was 44.63 m^3/g, 0.170 cc/g and 1.77 nm respectively. The higher the surface area of the NCs possesses higher active site for the effective interaction with organic pollutant which enhances the photocatalytic activity of the nanomaterial.

Uv–visible DRS

Kubelka Munk plot was used to determine the bandgap energy of the prepared nanomaterials [53]. The bandgap energy of Ag-r-GO-CFO-FO NCs, CFO and FO NPs were 2.48, 1.75 and 2.28 eV respectively (Supplementary material Fig. S1c). The coupling of nanomaterial with quandary heterojunction shifts the bandgap energy of the NCs towards the visible range, which enhances the photocatalytic efficiency of the NCs. In addition, Urbach energy of the fabricated nanomaterial was determined by Equ. 5.

$$\propto = \propto_0 + \exp \frac{E}{E_u} \quad (5)$$

where Eu, E and α denoted the Urbach energy, energy of the photon (hc / λ) and absorption coefficient respectively; α_0 is 4πk/ λ (k is ab-

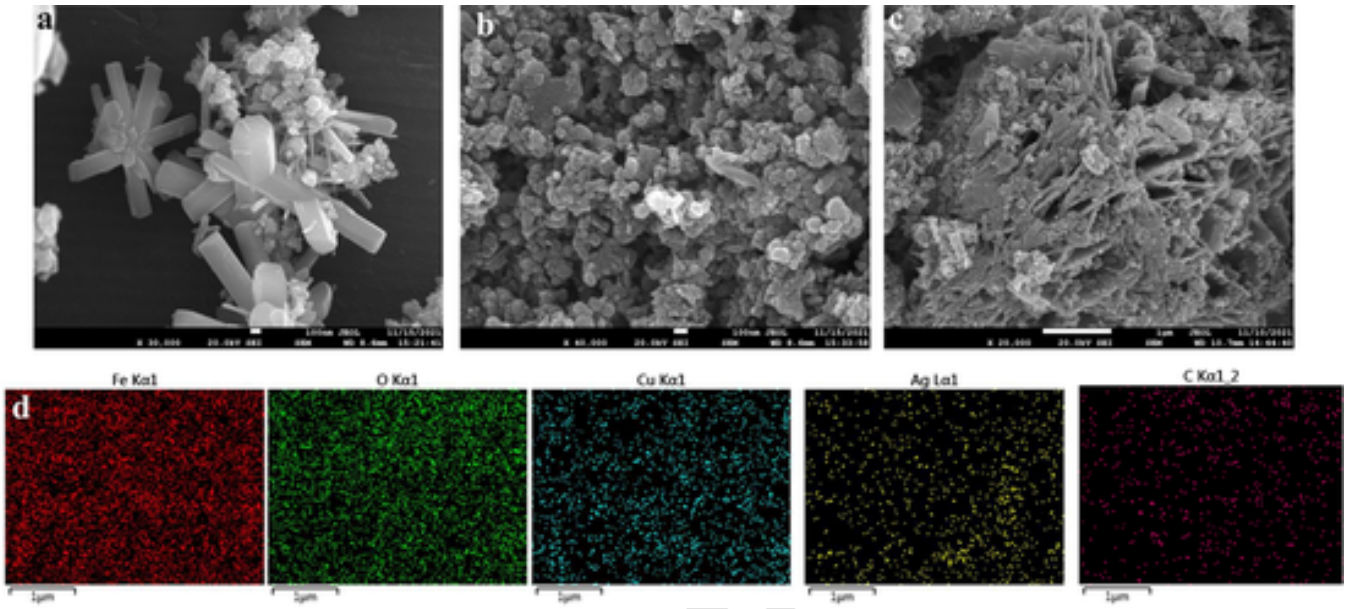

Fig. 2. SEM image of CFO_4 (a), FO (b), Ag-r-GO-CFO-FO NCs (c) and elemental mapping of Ag-r-GO-CFO-FO NCs (d).

sorbance and λ is wavelength). The Urbach energy of the CFO, FO and Ag-r-GO-CFO-FO NCs was 0.28, 0.36 and 0.192 eV respectively. The higher the Urbach energy of the NCs than the pure NPs which indicate the point defect on Ag-r-GO-CFO-FO NCs up on heterojunction formation. Here, the electronic structure (conduction band (CB) and valance band (VB)) was determined by Equ. 6 and 7 [54,55].

$$E_{VB} = X - E_C - \frac{1}{2}E_g \quad (6)$$

$$E_{CB} = E_{VB} - E_g \quad (7)$$

where, X is the electronegativity, E_c is the energy of the free electron and Eg is the band gap energy of the nanomaterial. The valance band (VB) and the conduction band (CB) of CFO are −0.69 and 1.15 eV, and Fe_3O_4 are 0.25 and 2.26 eV respectively.

Photoluminescence (PL)

The rate of recombination of the nanomaterial was determined by the photoluminescence spectroscopy (Fig. 3c). The lower in the PL intensity was observed with Ag-r-GO-CFO-FO NCs than pure CFO and FO NPs. The result shows the decreased recombination rate of NCs as compared to the pure CFO and FO NPs. PL spectrum showed peaks at 532, 622 and 653 nm corresponds to O 1S of band energy (3 eV) [56]. The surface defect of CeO_2 nanomaterial showed an emission spectrum in the range of 320 to 550 nm [56]. Similarly, Meng et al. 2019 determined the lattice defect of CeO_2 by performing PL spectroscopy and they observed that the electron mobilization of O 2p enables the effective photocatalytic performance [57]. In addition, they have observed that the peak broadening in the range of 450 to 550 nm was due to the defect state formation of the nanomaterial (lattice defect). The peak broadening at 552 nm shows the formation of lattice defect on Ag-r-GO-CFO-FO NCs [57].

Electrochemical impedance spectroscopy (EIS)

EIS of CFO, FO and Ag-r-GO-CFO-FO NCs are illustrated in Fig. 3d. Here. The Nyquist plot and bode plot of the nanomaterials shows that the higher the arc radius of pure CFO and FO NPs than Ag-r-GO-CFO-FO NCs. The higher the arc radius indicates the lower the resistance of the nanomaterial [58–60]. The higher the arc radius indicates the higher the resistance of the nanomaterial and thus the rate of recombination of the charge carrier is inversely proportional to the resistance of the nanomaterial [61,62]. The results conclude that the rate of recombination of Ag-r-GO-$CuFe_2O_4$ NCs was lower than pure $CuFe_2O_4$ and Fe_3O_4 NPs.

XPS

XPS analysis of the prepared Ag-r-GO-CFO-FO NCs is illustrated in Fig. 4. The sharp peak at 710.11 and 723.52 3 V corresponds to Fe which attribute to the electronic spin of $2p_{3/2}$ and $2p_{1/2}$ respectively with the oxidation state of + 2 [50]. The sharp peak at 528.57, 530.31 and 532.15 eV correspond to O with the electron spin 1S represents the metal–oxygen bond, surface oxygen and OH bond with oxidation state of −2 [50]. Here, the peak at 367.01 and 372.91 eV corresponds to Ag which attributes the electronic spin of $3d_{5/2}$ and $3d_{3/2}$ respectively [57]. The XPS spectrum of Cu showed sharp peaks at 933.77 and 953.86 eV attributed to the electronic spin of $2p_{3/2}$ and $2p_{1/2}$ respectively. The peaks at 942.02 and 961.63 eV were the satellite peaks of Cu [50]. The peak at 283.48 eV corresponds to carbon (1S), which further confirms the presence of r-GO [63]. Thus, the XPS spectra further confirm the formation of Ag-r-GO-CFO-FO NCs.

Photocatalytic degradation of industrial dye

The photocatalytic degradation of red RB, orange 2R and black B (100 mg/L) was augmented with 20 mg/L of nanomaterial and kept in an orbital shaker for 30 min. The optical density of the reaction mixture before the adsorption was measured to determine the adsorption effect and it showed very negligible adsorption of pollutants on NCs (Supplementary material Fig. S2). The results show that the degradation efficiency of red RB by r-GO-CFO-FO-10, r-GO-CFO-FO-20 and r-GO-CFO-FO-30 was calculated to be 90.2, 71.1 and 55.1 % respectively. The degradation efficiency of orange 2R by r-GO-CFO-FO-10, r-GO-CFO-FO-20 and r-GO-CFO-FO-30 was calculated to be 90.7, 56.3 and 45.6 % respectively. The degradation efficiency of black B by r-GO-CFO-FO-10, r-GO-CFO-FO-20 and r-GO-CFO-FO-30 was calculated to be 87.3, 58.8 and 42.5 % respectively in 120 min (Supplementary material Fig. S3). The results show that the r-GO-CFO-FO-10 showed effective photocatalytic degradation of the organic dyes than CFO-FO-20 and r-GO-CFO-FO-30. Further, r-GO-CFO-FO-10 nanomaterial was decorated by Ag NPs as Ag-r-GO-CFO-FO-1, Ag-r-GO-CFO-FO-3, Ag-r-GO-CFO-FO-5 and the degradation efficiency was calculated. Here, the degradation efficiency of red RB by Ag-r-GO-CFO-FO-1, Ag-r-GO-CFO-

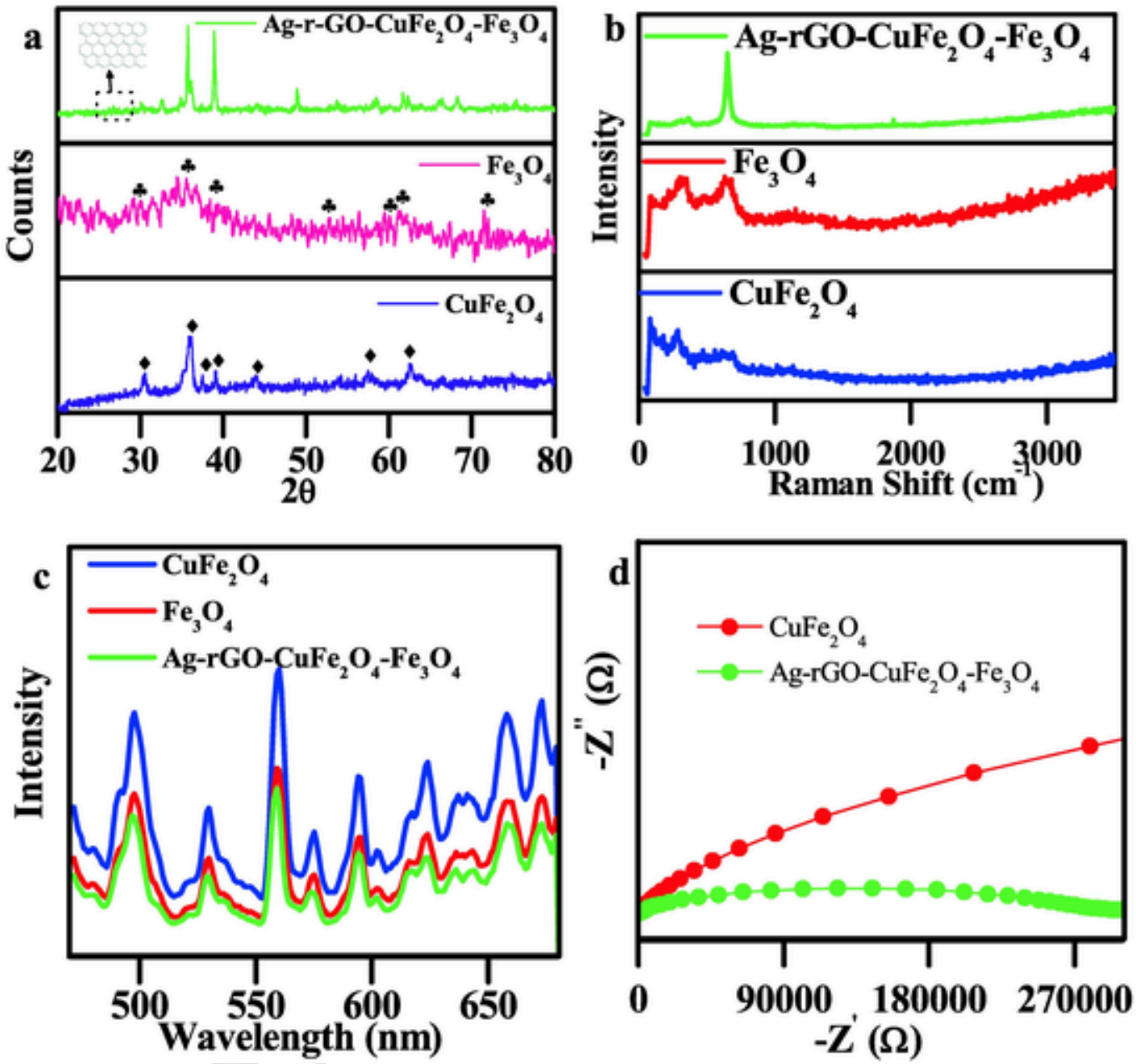

Fig. 3. XRD (a), Raman (b), photoluminescence (c) and electron impendence spectroscopy (d) of CFO, FO and Ag-r-GO-CFO-FO NCs.

FO-3 and Ag-r-GO-CFO-FO-5 was calculated to be 57.1, 57.7 and 99.8 % respectively. The degradation efficiency of orange 2R by Ag-r-GO-CFO-FO-1, Ag-r-GO-CFO-FO-3 and Ag-r-GO-CFO-FO-5 was calculated to be 78.1, 85.5 and 99.3 % respectively. The degradation efficiency of black B by Ag-r-GO-CFO-FO-1, Ag-r-GO-CFO-FO-3 and Ag-r-GO-CFO-FO-5 was calculated to be 45.5, 51.6 and 99.8 % respectively in 120 min. The results show that the photocatalytic degradation of the organic dyes was effective by Ag-r-GO-CFO-FO-5. The higher the decoration of Ag above 5 % decreases the efficiency which might be due to the screening effect. The higher the decoration of Ag blocks the reactive site of r-GO-CFO-FO which results in the lower interaction with the dye and thus inhibits the degradation process (Fig. 5). In addition, the photocatalytic efficiency of pure r-GO, CFO, FO, Ag, r-GO-CFO and CFO-FO NCs was studied and the degradation efficiency of red RB by r-GO, CFO, FO, Ag, r-GO-CFO and CFO-FO NCs was calculated to be 51.0, 55.7, 49.1, 64.3, 68.2 and 62.6 % respectively. The degradation efficiency of orange 2R by r-GO, CFO, FO, Ag, r-GO-CFO and CFO-FO NCs was 55.4, 52.9, 51.1, 69.4, 57.4 and 61.5 % respectively. The degradation efficiency of Black B by r-GO, CFO, FO, Ag, r-GO-CFO and CFO-FO NCs was 52.0, 61.2, 61.4, 61.5, 63.6 and 69.8 % respectively (Fig. 5). The complete mineralization of red RB, orange 2R and black B was determined by estimating the total organic carbon (TOC). The TOC remaining after the degradation of red RB, orange 2R and black B by Ag-r-GO-CFO-FO NCs were 2.1, 1.6 and 1.9 % respectively, which shows the complete mineralization of dye by Ag-r-GO-CFO-FO NCs under visible light irradiation. The rate kinetic reaction on the photocatalytic activity of nanomaterial against red RB, orange 2R and black B was determined by Equ. 8.

$$\ln\left(\frac{C}{C_0}\right) = Kt \tag{8}$$

where, K represent the rate constant, C and C_0 represent the initial and final concentration of the organic dye. The rate constant of Ag-r-

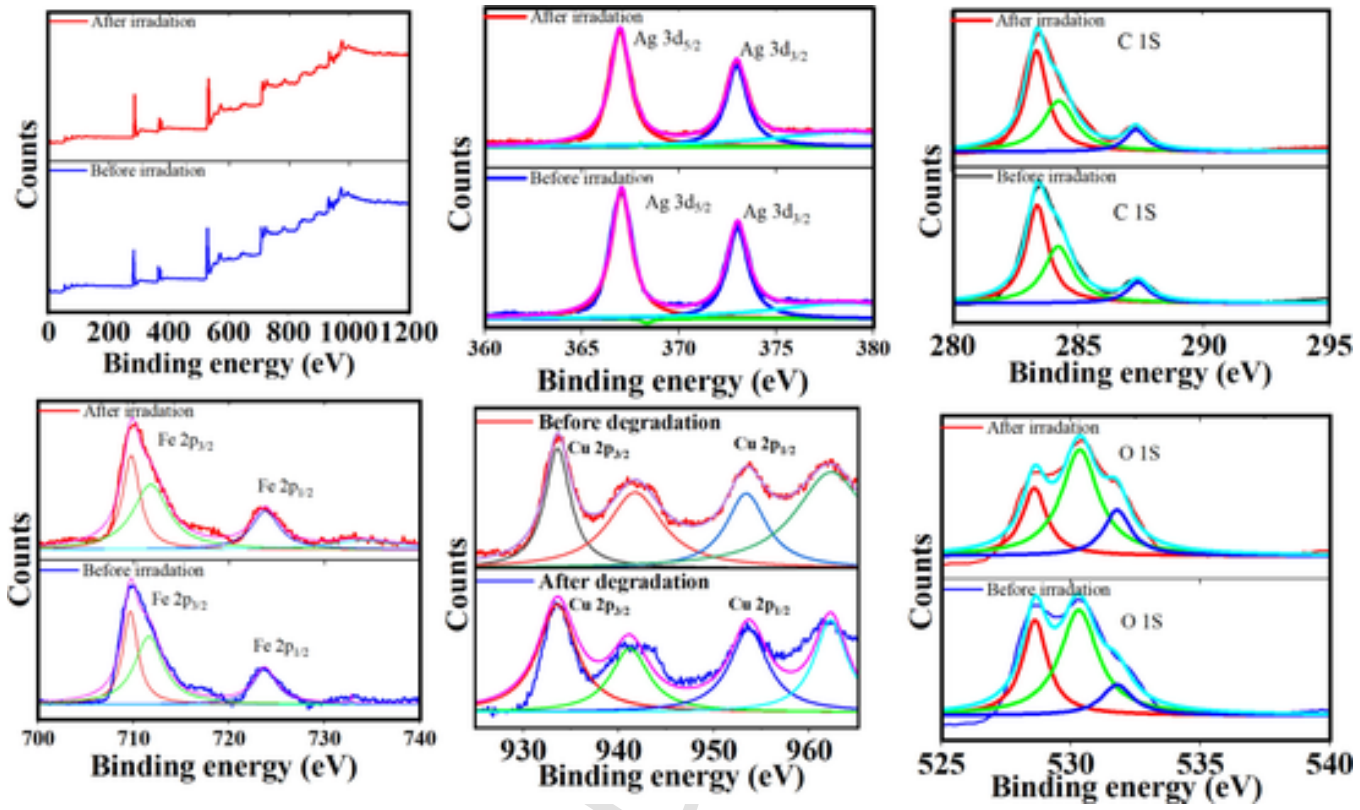

Fig. 4. XPS spectrum of Ag-r-GO-CFO-FO NCs before and after irradiation.

GO-CFO-FO NCs was higher than the pure r-GO, CFO, FO and Ag NPs, which further confirms the photocatalytic efficiency of NCs (Supplementary material Table S1). The regression coefficient of the photocatalytic degradation of the organic pollutants was higher than 0.95 and the reaction follows pseudo first-order reaction.

Similarly, the photocatalytic degradation of red RB, orange 2R and black B by different concentrations of NCs from 5 to 25 mg/L was studied. The results show that photocatalytic degradation was higher at 25 mg/L concentration of NCs (Supplementary material Fig. S4). In addition, the photocatalytic degradation of NCs (20 mg/L) was studied at different concentrations of red RB, orange 2R and black B from 50 to 150 mg/L (Supplementary material Fig. S5). The results show that the photocatalytic activity of NCs was effective at 50 mg/L of organic pollutants. According to the Langmuir-Hinshelwood (L-H) model, the increase in the concertation of nanomaterial, changes the rate of the reaction from pseudo first-order kinetic to zero-order kinetic. The change in the rate kinetic occurs when there is excess reactive surface of the NCs available with respect to dye. The study shows no change in the rate kinetics which indicates that photocatalytic degradation didn't follow LH model. Further, the degradation efficiency was studied by varying pH from 4 to 9, and the results show that the degradation was higher at pH 7. Here, the pKa value of the red RB, orange 2R and black B dyes was found to be 6.5, 8.26 and 6.9 respectively and the isoelectric point (IEP) of the NCs was found to 7.1. The IEP of NCs falls closely to the pKa values of all three dyes which enables the effective interaction for the complete degradation of organic dyes.

Real sample analysis

The real time application was studied by performing the photocatalytic activity of Ag-r-GO-CFO-FO NCs against industrial effluent (combination of red RB, orange 2R and black B). Briefly industrial effluent (100 mg/L) was augmented with 20 mg/L of nanomaterial and kept it orbital shaker for 30 min. Then the solution was irradiated. Fig. 6a shows the UV–visible absorption spectrum of the photocatalytic degradation of industrial effluent against Ag-r-GO-CFO-FO NCs. The degradation efficiency of the industrial effluent by Ag-r-GO-CFO-FO NCs was calculated to be 98.2 % with a rate constant of 0.40 min^{-1} and R^2 was higher than 0.95, which shows the reaction follows pseudo first-order kinetics.

Reusability and scavenging

The reusability study was performed by six cycle test on the photocatalytic degradation of red RB, orange 2R and black B by Ag-r-GO-CFO-FO NPs. The reusability efficiency was found to be 99, 99.5 and 99.4 % respectively (Fig. 6c). In addition, the photocorrosion of the NCs was studied by performing XPS of NCs after irradiation (Fig. 4). The XPS results show that there is no shift in the peak and no loss in the peak intensity was observed indicate the stability of NCs after photodegradation. Radical scavenging experiment was performed by the addition of $AgNO_3$, EDTA, BQ and IPA to the reaction mixture and the results show that lower in degradation efficiency was observed on BQ and IPA for all three organic pollutants (Fig. 6b). IPA and BQ captures the formed •OH and O_2•- respectively and thus inhibits the interaction of the radical with dye [64,65]. The degradation efficiency of dye was calculated in the scavenging experiment indicates that •OH and O_2•- plays a major role in the photocatalysis. In addition, electron spin resonance spectroscopy was performed in the presence of 5,5,-dimethylpyrroline-N-oxide (DMPO), 5-tertbutoxycarbonyl-5-methyl-1-pyroline-N-oxide (BMPO) and 5-diethoxyphosphoryl-5-methyl-1-pyrroline-N-oxide (DEPMPO) and they have been used as spin traps for oxygen centered free radicals. The ESR spectrum of Ag-r-GO-CFO-FO NCs was higher than the pure CFO and FO NPs, which conform to the effective formation of •OH and • O_2•- (Supplementary material Fig. S6).

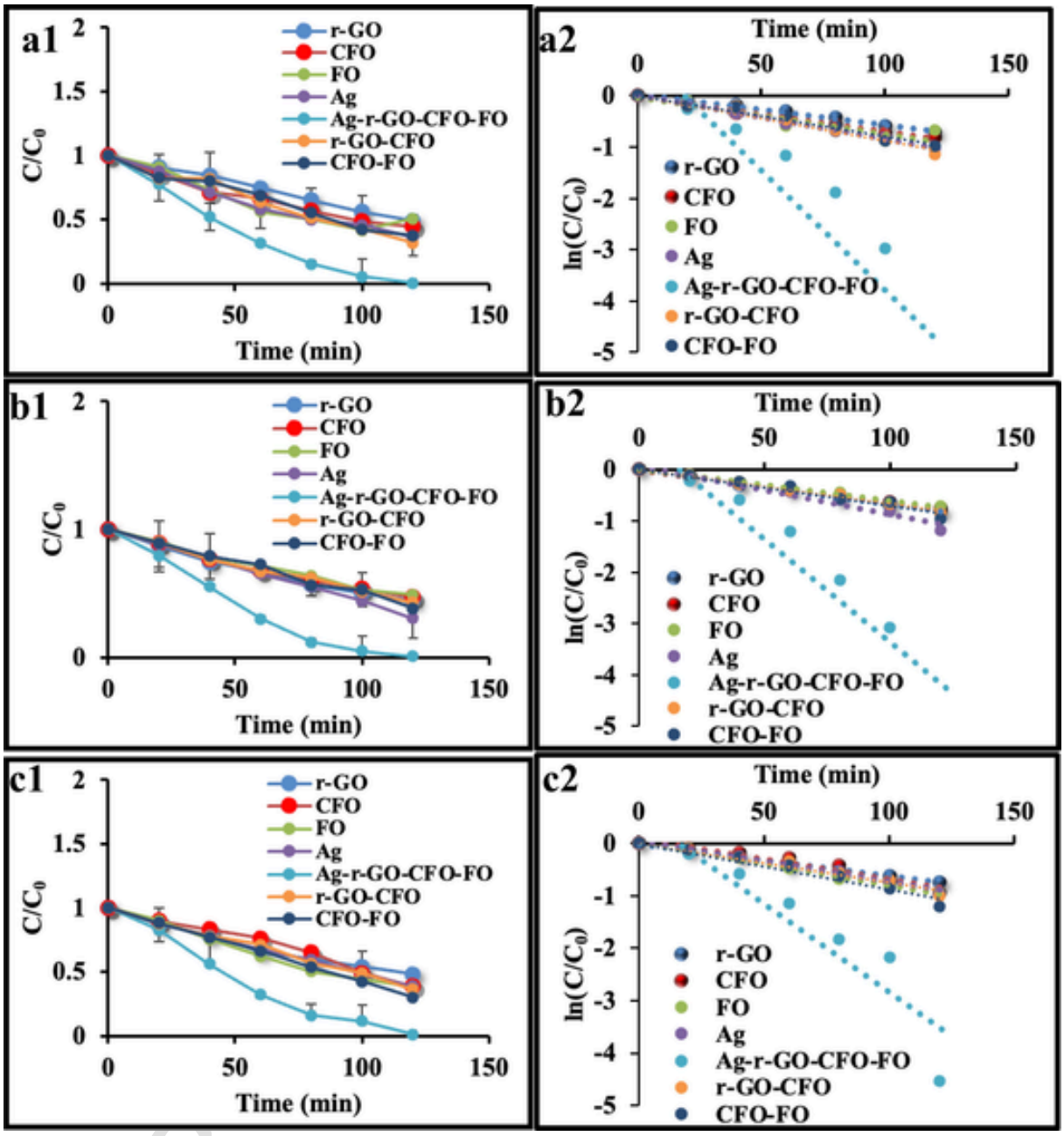

Fig. 5. Plot on C/C_0 and $\ln(C/C_0)$ at different nanomaterial (r-GO, Ag, CFO, FO, Ag-rGO-CFO-FO NCs) against organic dye. Red RB (a_1 & a_2), orange 2R (b_1 & b_2) and black B (c_1 & c_2) (NCs – 20 mg/L, pollutant – 100 mg/L at pH 7). (For interpretation of the references to colour in this figure legend, the reader is referred to the web version of this article.)

Photocatalytic mechanism of Ag-r-GO-CFO-FO NCs

The photocatalytic mechanism of Ag-r-GO-CFO-FO NCs against the organic dye is illustrated in Fig. 7. The VB and CB of CFO is −0.69 and 1.15 eV, and FO is 0.25 and 2.26 eV respectively. The work function (Φ) of Ag, r-GO, CFO and FO was 4.2, 4.1, 3.64 and 3.85 eV respectively. Here, the work function of the r-GO was lower than the CFO, and the electron transfers from electron-rich r-GO pumps to CFO which in term forms the Ohmic junction. The investigation revealed that the interfacial electric field plays a crucial role in propelling the photogenerated carriers across the Schottky barrier, thereby significantly enhancing the electron transfer rate at the interface of Ag-r-GO-CFO-FO NCs [66–68]. Mott-Schottky plot of CFO and FO determines n and p type semiconductor [69]. The result shows that flat-band potential (U_{fb}) of CFO and FO were 0.97 and −0.26 V respectively which indicates the p-type CFO and n-type FO semiconductor (Supplementary material Fig. S1d). Here, the coupling of CFO and FO intends in the formation of an interfacial Schottky barrier (Schottky-like junction) to facilitate the effective charge transfer between the photosystems. The charge down flow in the NCs forms two interfacial charge separations on both Ohmic junction and Schottky junction. Here, the conduction band potential is higher than −0.18 eV (NHE O_2 to O_2•-) which enables the effective formation of O_2•- radical [70,71]. The higher the positive potential in VB of FO (1.99 eV), which converts the OH^- to •OH. The formation of O-S chain mechanism of Ag-r-GO-CFO-FO NCs shows the effective formation of •OH and O_2•- for the complete mineralization of the organic pollutant.

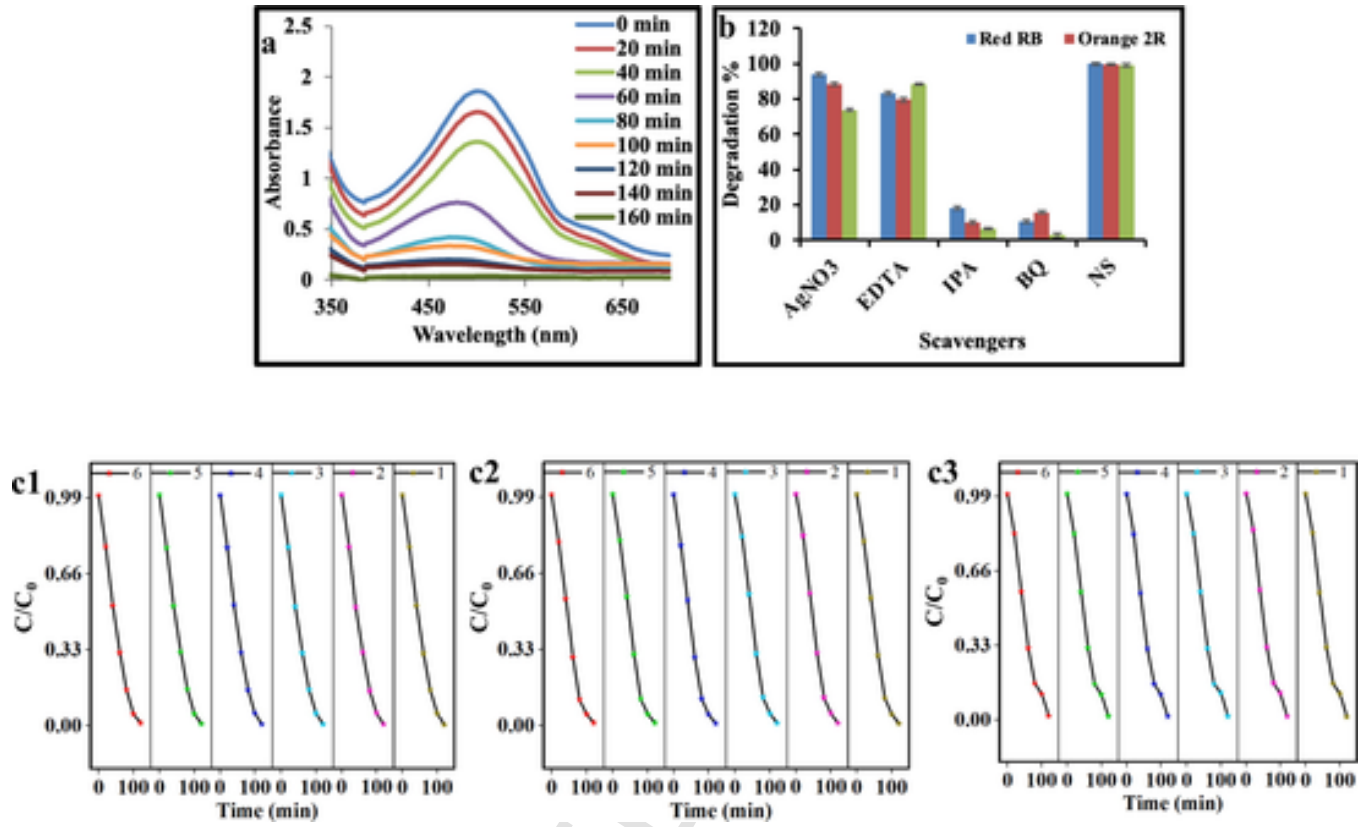

Fig. 6. UV–visible absorption spectra of photocatalytic degradation of industrial effluent against Ag-r-GO-CFO-FO NCs (a), radical quenching (b) and reusability test in presence of red RB (c_1), orange 2R (c_2) and black B (c_3) (NCs – 20 mg/L, Pollutant – 100 mg/L at pH 7). (For interpretation of the references to colour in this figure legend, the reader is referred to the web version of this article.)

Photocatalytic degradation pathway on the degradation of organic pollutant

The photocatalytic degradation mechanism on the mineralization of organic pollutants (red RB, orange 2R and black B) was determined by GC–MS analysis (Supplementary material Fig. S7, Fig. S8 & Fig. S9). The electronic density on the coupling of Ag-r-GO, FO and CFO was found to be higher in NCs than pure NPs. The nucleophilic and electrophilic attack on the organic pollutant (red RB, orange 2R and black B) breaks the bond and thus forms the intermediate product by Ag-r-GO-CFO-FO NCs under visible light irradiation. Here, the radical attack occurs on the N = N in the benzene ring of all three organic pollutants and then cleaves the benzene ring leads to the formation of the intermediate compounds. Further, photo-oxidation and photo-reduction of organic pollutant leads to the formation of CO_2, H_2O and SO_4.

Toxicity on plants

Nanocomposites improved the biomass accumulation and photosynthetic rate of Trifolium seedlings

Form the data illustrated in Fig. 8, it is obvious that the treatment of Trifolium plants with γ-GO, $CuFe_2O_3$, Fe_3O_4 separately either significantly reduced the fresh and dry weights of plants, particularly at the high concentrations (100 mg/L) or did not induce a significant effect (Supplementary material Table S2). On the other hand, the application of Ag-r-GO-CFO-FO NCs significantly improved the growth rate of Trifolium plants represented by fresh and dry weights. This improvement was in direct proportion with the concentration of the nanocomposite.

The heightened chlorophyll levels concurrently influence photosynthetic efficiency, showing an increase in *Trifolium* subjected to both individual NPs and NCs in both low and high dosages. The most notable impact was observed in plants treated with the NCs (Supplementary Material Fig. S10). In summary, our findings indicate that treatment with individual nanomaterials (r-GO, CFO, and FO) did not result in a substantial improvement in chlorophyll content. Conversely, the application of Ag-rGO-CFO-FO NCs resulted in a significant enhancement in chlorophyll content and, consequently, an improved photosynthesis rate compared to untreated control plants.

Nanocomposites enhanced the total antioxidant capacity and accumulation of antioxidants in Trifolium plants

Regarding the total antioxidant capacity and antioxidant metabolites, it was noticeable from Supplementary material Fig. S10 that the treatment with r-GO, FO, and Ag-r-GO-CFO-FO NCs significantly boosted the antioxidant capacity of *Trifolium* plants, when compared to untreated groups ($p < 0.05$), which reflects the oxidative stress effect caused by these nanomaterials (Supplementary material Table S3). However, there were no significant differences between the two concentrations of the same nanomaterial. On the contrary, the effect of CFO, on the TAC was comparable to control groups. Concerning phenol contents, there were no significant differences between r-GO and CFO on one side and control group on the other side. Whereas, FO and Ag-r-GO-CFO-FO NCs were significantly reduced the levels of polyphenols in *Trifolium* plants ($p < 0.05$) in comparison with untreated and CFO-treated groups. As regards flavonoids, CFO did not induce a noticeable impact on their levels when compared to untreated samples. On the other hand, r-GO, FO, and Ag-r-GO-CFO-FO NCs significantly boosted the levels of flavonoids, Ag-r-GO-CFO-FO NCs had the greatest impact (Supplementary material Fig. S10).

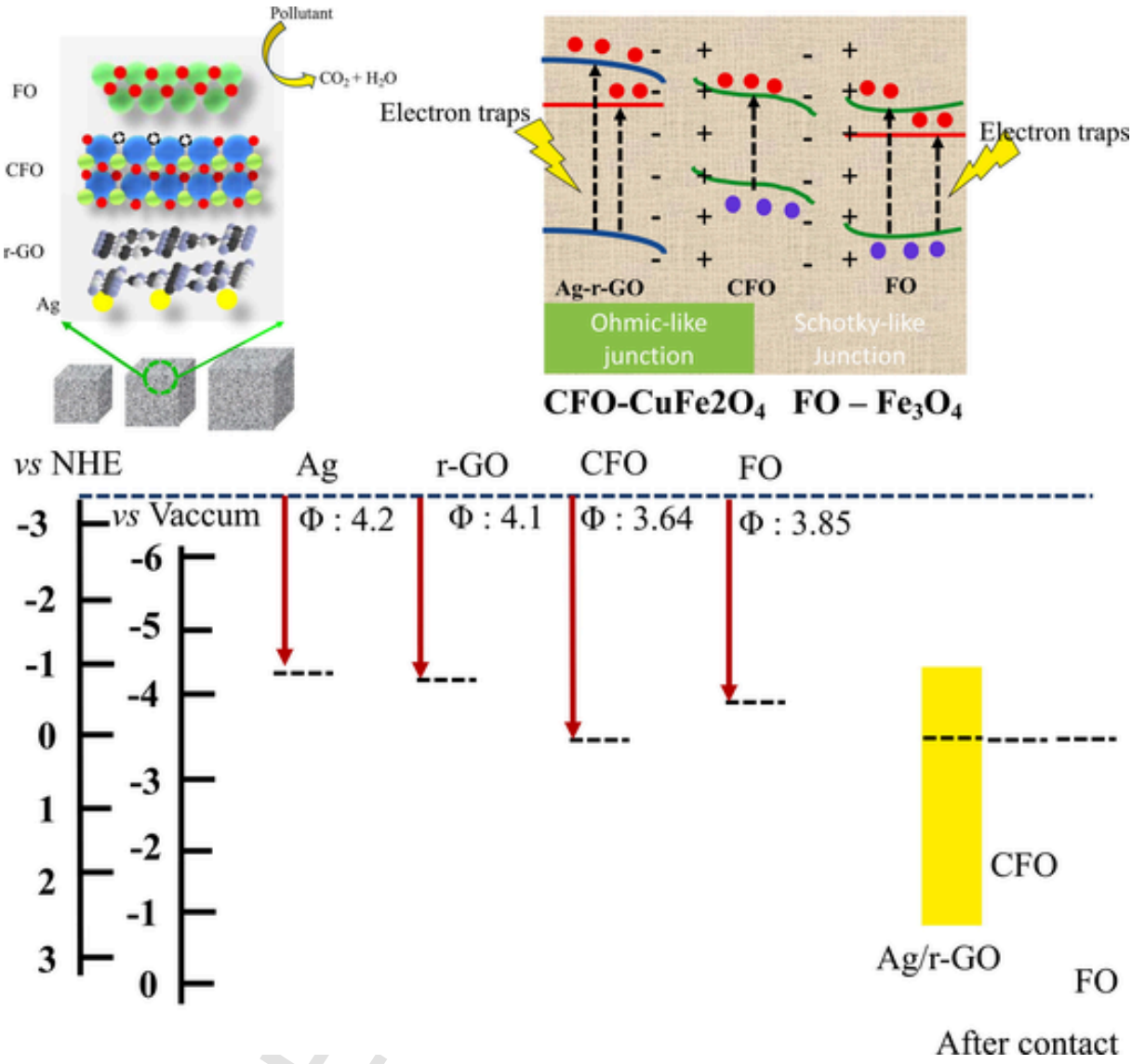

Fig. 7. Photocatalytic mechanism of Ag-r-GO-$CuFe_2O_4$-Fe_3O_4 NCs.

Ag-r-GO-CFO-FO NCs improved the accumulation of minerals in Trifolium seedlings

Another important factor in the nutritional quality of plants is the levels of mineral elements. Therefore, we, herein, determined the levels of N, P, K, Fe, Zn, and Mg in r-GO, CFO, FO, and Ag-r-GO-CFO-FO NCs-treated and untreated *Trifolium* plants. Apparently, r-GO showed the most positive effect on the levels of minerals, as Trifolium plants treated with r-GO had the highest values of N, P, K and mg, while the highest concentrations of Fe and Zn were reported in CFO- treated groups. In general, treatment with CFO, and FO, and Ag-r-GO-CFO-FO NCs had a reducing effect on the accumulation of mineral elements in Trifolium plants.

Conclusions

In summary, we report the Ohmic and Schottky junction (O-S scheme) Ag-r-GO-CFO-FO NCs for effective photocatalytic activity against organic pollutants. Here, the coupling of the high positive potential conduction band ($CuFe_2O_4$) with the high negative potential valance band (Fe_3O_4) intends in the formation of an interfacial Schottky barrier (Schottky-like junction) to facilitate the effective charge transfer between the photosystems. Meanwhile, the coupling of Ag-r-GO with the Schottky-like junction is expected to form ohmic contact (Ohmic like junction). Ohmic junction acts as an electron trap and pumps the electron from Ag-r-GO to the Schottky junction (CFO-FO) which facilitates the effective photo-oxidation and photo-reduction of O_2 and OH^-. The photocatalytic activity of the constructed Ag-r-GO-CFO-FO NCs was tested against organic industrial pollutants (red RB, orange 2R and black B) and the degradation efficiency was calculated to be 99.8, 99.3 and 99.8 %, where •OH and O_2•- plays a major role in the reaction. The reusability efficiency of the nanomaterial was found to be prominent and stable after six consecutive cycles, which shows that the nanomaterial didn't undergrow photo-corrosion. The new-fashioned O-S scheme mechanism on the coupling photosystem boosts the charge transfer for the effective photocatalytic activity of the nanomaterial.

Declaration of competing interest

The authors declare that they have no known competing financial interests or personal relationships that could have appeared to influence the work reported in this paper.

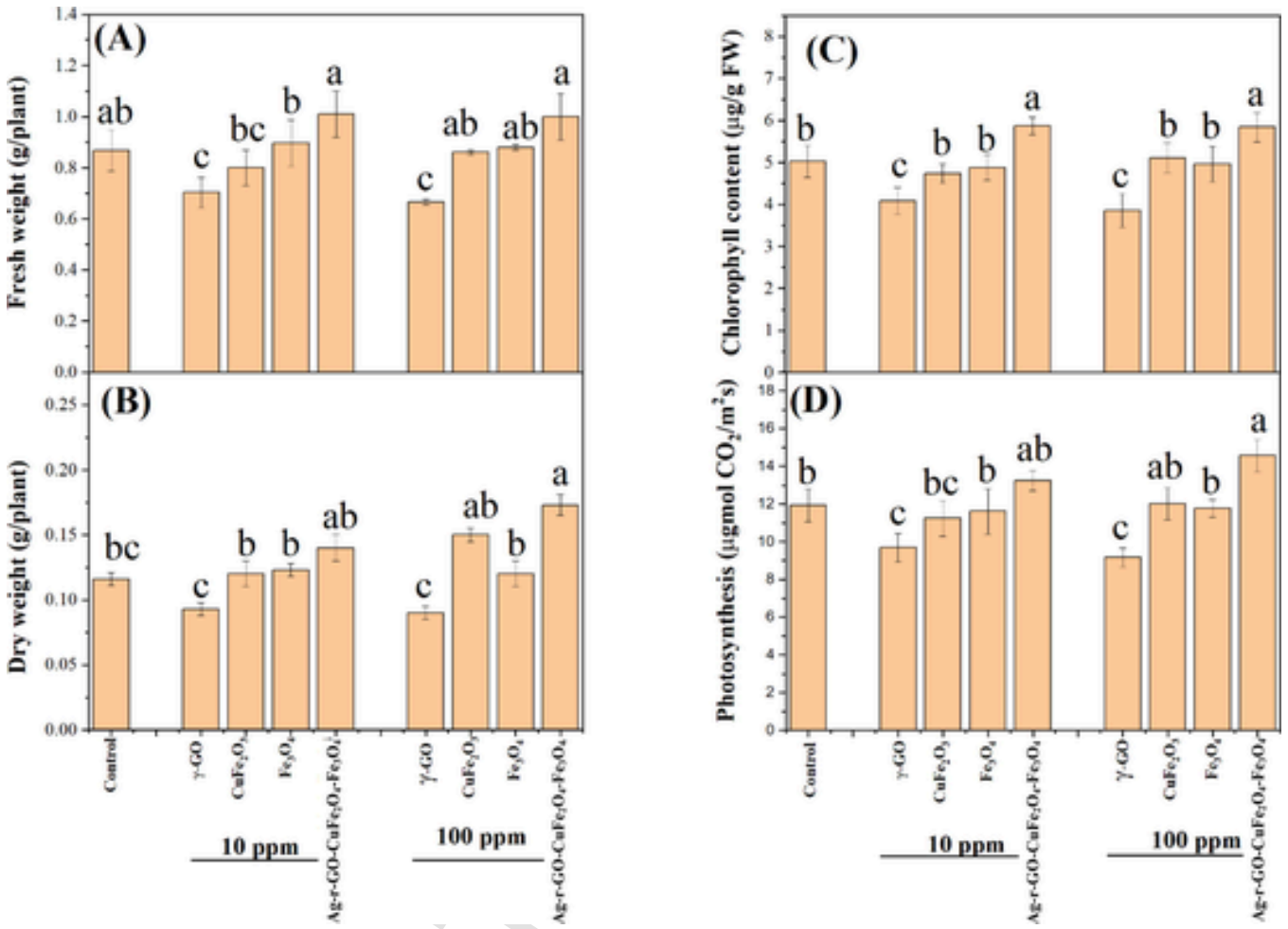

Fig. 8. Effect of r-GO, CFO, FO and Ag-r-GO-CFO-FO NCs nanomaterials at two concentrations (10 and 100 mg/L) on the biomass (fresh and dry weight) as well as photosynthesis of Trifolium plants. Data are represented by the means of four independent replicates and error bars represent the standard error. Different letters on each bar indicate significant difference ($p < 0.05$) between treatments.

Acknowledgments

The authors extend their appreciation to the Researchers Supporting Project number (RSP2023R176) King Saud University, Riyadh, Saudi Arabia.

Appendix A. Supplementary material

Supplementary data to this article can be found online at https://doi.org/10.1016/j.jiec.2024.01.046.

References

[1] J. Zuo, S. Bonyadi, T.S. Chung, Exploring the potential of commercial polyethylene membranes for desalination by membrane distillation, J. Membrane Sci. 497 (2016) 239–247.
[2] Y.Y. Qin, H. Li, J. Lu, F.Y. Meng, C.C. Ma, Y.S. Yan, M.J. Meng, Nitrogen-doped hydrogenated TiO_2 modified with CdS nanorods with enhanced optical absorption, charge separation and photocatalytic hydrogen evolution, Chem. Eng. J. 384 (2020).
[3] A. Nezamzadeh-Ejhieh, M. Shahanshahi, Modification of clinoptilolite nano-particles with hexadecylpyridynium bromide surfactant as an active component of Cr(VI) selective electrode, J. Ind. Eng. Chem. 19 (2013) 2026–2033.
[4] A. Nezamzadeh-Ejhieh, S. Khorsandi, Photocatalytic degradation of 4-nitrophenol with ZnO supported nano-clinoptilolite zeolite, J. Ind. Eng. Chem. 20 (2014) 937–946.
[5] G.Z. Zuo, R. Wang, Novel membrane surface modification to enhance anti-oil fouling property for membrane distillation application, J. Membrane Sci. 447 (2013) 26–35.
[6] Z.L. Chen, D. Rana, T. Matsuura, Y.F. Yang, C.Q. Lan, Study on the structure and vacuum membrane distillation performance of PVDF composite membranes: I. Influence of blending, Sep. Purif. Technol. 133 (2014) 303–312.
[7] A. Nezamzadeh-Ejhieh, N. Moazzeni, Sunlight photodecolorization of a mixture of Methyl Orange and Bromocresol Green by CuS incorporated in a clinoptilolite zeolite as a heterogeneous catalyst, J. Ind. Eng. Chem. 19 (2013) 1433–1442.
[8] A. Nezamzadeh-Ejhieh, M. Khorsandi, A comparison between the heterogeneous photodecolorization of an azo dye using Ni/P zeolite and NiS/P zeolite catalysts, Iranian, J. Catal. 1 (2011) 99–104.
[9] S. Vahabirad, A. Nezamzadeh-Ejhieh, M. Mirmohammadi, The coupled BiOI/$(BiO)_2CO_3$ catalyst: Brief characterization, and study of its photocatalytic kinetics, J. Solid State Chem. 314 (2022) 123405.
[10] Q. Cheng, Y.J. Yuan, R. Tang, Q.Y. Liu, L. Bao, P. Wang, J.S. Zhong, Z.Y. Zhao, Z.T. Yu, Z.G. Zou, Rapid hydroxyl radical generation on (001)-facet-exposed ultrathin anatase TiO_2 Nanosheets for enhanced photocatalytic lignocellulose-to-H_2 conversion, ACS Catal. 12 (2022) 2118–2125.
[11] J.J. Zhang, Y. Zhao, K.Z. Qi, S.Y. Liu, CuInS2 quantum-dot-modified g-C_3N_4 S-scheme heterojunction photocatalyst for hydrogen production and tetracycline degradation, J. Mater. Sci. Technol. 172 (2024) 145–155.
[12] J.H. Song, J.J. Zhang, K.Z. Qi, C. Imparato, S.Y. Liu, Exploration of the g-C_3N_4 Heterostructure with Ag-In Sulfide quantum dots for enhanced photocatalytic activity, ACS Appl. Electron. Mater. 5 (2023) 4134–4144.
[13] X.W. Ruan, X.Q. Cui, Y. Cui, X.F. Fan, Z.Y. Li, T.F. Xie, K.K. Ba, G.R. Jia, H.Y. Zhang, L. Zhang, W. Zhang, X. Zhao, J. Leng, S.Y. Jin, D.J. Singh, W.T. Zheng, Favorable Energy band alignment of TiO_2 Anatase/rutile heterophase homojunctions yields photocatalytic hydrogen evolution with quantum efficiency exceeding 45.6%, Adv. Energy. Mater. 12 (2022) 2200298.
[14] M. Swedha, S. Balasurya, A. Syed, S. Arunava Das, S. Khan, Continuous photocatalysis via Z-scheme based nanocatalyst system for environmental remediation of pharmaceutically active compound: Modification, reaction site, defect engineering and challenges on the nanocatalyst, J. Mol. Liq. 353 (2022) 118745.
[15] Q.F. Cui, Y. Zhao, K.Z. Qi, Y. Yan, S-scheme CuInS$_4$/ZnS heterojunctions for the visible light-driven photocatalytic degradation of tetracycline antibiotic drugs, J Taiwan Inst Chem E 142 (2023).

[16] J.J. Zhang, X.Y. Gu, Y. Zhao, K. Zhang, Y. Yan, K.Z. Qi, Photocatalytic Hydrogen production and tetracycline degradation using $ZnIn_2S_4$ Quantum dots modified g-C_3N_4 composites, Nanomaterials 13 (2023) 305.

[17] Z.R. Yang, J.Y. Zhang, W.T. Zhang, Q. Zhou, J.Y. Shen, Y. Huang, Stearic acid modified Co^{2+}-doped ZnO: The construction of micro-nano structure for its superhydrophobic performance and visible-light photocatalytic degradation of methylene blue, J. Clean. Prod. 382 (2023).

[18] Z. Wu, X.L. Wang, X. Wang, X.F. Xu, D.S. Li, T. Wu, 0D/2D heterostructure constructed by ultra-small chalcogenide-cluster aggregated quaternary sulfides and g-C_3N_4 for enhanced photocatalytic H_2 evolution, Chem. Eng. J. 426 (2021).

[19] C.H. Deng, L.L. Peng, X.H. Ling, T. Wang, R. Xu, Y.B. Zhu, C.C. Wang, X.H. Qian, L.L. Wang, Y.P. Wu, H.M. Hu, Y.S. Han, Construction of S-scheme Zn0.2Cd0.8S/biochar aerogel architectures for boosting photocatalytic hydrogen production under sunlight irradiation, J. Clean. Prod. 414 (2023).

[20] A. Nezamzadeh-Ejhieh, H. Zabihi-Mobarakeh, Heterogeneous photodecolorization of mixture of methylene blue and bromophenol blue using CuO-nano-clinoptilolite, J. Ind. Eng. Chem. 20 (2014) 1421–1431.

[21] A. Nezamzadeh-Ejhieh, A. Yousefi, Preperation and characterization of SnO_2-$BiVO_4$-CuO catalyst and kinetic phenazopyridine photodegradation, Iran. J. Catal. 11 (2021) 247–259.

[22] S. Park, J.H. Baek, L. Zhang, J.M. Lee, K.H. Stone, I.S. Cho, J.H. Guo, H.S. Jung, X.L. Zheng, Rapid Flame-annealed $CuFe_2O_4$ as Efficient photocathode for photoelectrochemical hydrogen production, ACS Sustain. Chem. Eng. 7 (2019) 5867–5874.

[23] J.T. Bi, X. Huang, J.K. Wang, T. Wang, H. Wu, J.Y. Yang, H.J. Lu, H.X. Hao, Oil-phase cyclic magnetic adsorption to synthesize Fe_3O_4@C@TiO_2-nanotube composites for simultaneous removal of Pb(II) and Rhodamine B, Chem. Eng. J. 366 (2019) 50–61.

[24] S. Tamang, S. Rai, R. Bhujel, N.K. Bhattacharyya, B.P. Swain, J. Biswas, A concise review on GO, rGO and metal oxide/rGO composites: Fabrication and their supercapacitor and catalytic applications, J. Alloys Compd. 947 (2023) 169588.

[25] A.L. Mudarra, S.M. de Salinas, M.H. Pérez-Temprano, Beyond the traditional roles of Ag in catalysis: the transmetalating ability of organosilver(i) species in Pd-catalysed reactions, Org. Biomol. Chem. 17 (2019) 1655–1667.

[26] J.M. Wu, H.A. Shi, K.Y. Li, X.W. Guo, Advances and challenges of single-atom catalysts in environmental catalysis, Curr. Opin. Chem. Eng. 40 (2023) 100923.

[27] X.H. Wang, X.H. Wang, T.Y. Shi, A.L. Meng, T.Q. Yang, M.M. Zhang, L. Wang, G.C. Li, J.F. Huang, X. Yu, Z.J. Li, "O-S" Charge Transfer mechanism guiding design of a $ZnIn_2S_4$/$SnSe_2$/In_2Se_3 Heterostructure photocatalyst for efficient hydrogen production, ACS Catal. 13 (2023) 1020–1032.

[28] J.H. Song, J.J. Zhang, A. Zada, K.Z. Qi, Y.H. Ma, $CoFe_2O_4$/$NiFe_2O_4$ S-scheme composite for photocatalytic decomposition of antibiotic contaminants, Ceram. Int. 49 (2023) 12327–12333.

[29] K.Z. Qi, C.Q. Zhuang, M.J. Zhang, P. Gholami, A. Khataee, Sonochemical synthesis of photocatalysts and their applications, J. Mater. Sci. Technol. 123 (2022) 243–256.

[30] L.G.P. Tienne, L.D. Candido, B.D.M. da Cruz, F.F. Gondim, M.P. Ribeiro, R.A. Simao, M.D.V. Marques, S.N. Monteiro, Reduced graphene oxide synthesized by a new modified Hummer's method for enhancing thermal and crystallinity properties of Poly(vinylidene fluoride), J. Mater. Res. Technol. 18 (2022) 4871–4893.

[31] S.A. Mirsalari, A. Nezamzadeh-Ejhieh, A.R. Massah, A designed experiment for CdS-AgBr photocatalyst toward methylene blue, Environ Sci Pollut R 29 (2022) 33013–33032.

[32] K.Z. Qi, R. Selvaraj, T. Al Fahdi, S. Al-Kindy, Y. Kim, G.C. Wang, C.W. Tai, M. Sillanpää, Enhanced photocatalytic activity of anatase-TiO_2 nanoparticles by fullerene modification: A theoretical and experimental study, Appl. Surf. Sci. 387 (2016) 750–758.

[33] S.B. Bandgar, M.M. Vadiyar, U.P. Suryawanshi, C.L. Jambhale, J.H. Kim, S.S. Kolekar, Rotational reflux chemistry approach derived flat holey $CuFe_2O_4$ nanosheets for supercapacitors application, Mater Lett 279 (2020) 128514.

[34] A. Lak, D. Niculaes, G.C. Anyfantis, G. Bertoni, M.J. Barthel, S. Marras, M. Cassani, S. Nitti, A. Athanassiou, C. Giannini, T. Pellegrino, Facile transformation of FeO/Fe_3O_4 core-shell nanocubes to Fe_3O_4 magnetic stimulation, Sci. Rep. 6 (2016) 33295.

[35] P.K. Khanna, N. Singh, S. Charan, V.V.V.S. Subbarao, R. Gokhale, U.P. Mulik, Synthesis and characterization of Ag/PVA nanocomposite by chemical reduction method, Mater. Chem. Phys. 93 (2005) 117–121.

[36] B. Li, A.H. Amin, A.M. Ali, M. Isam, A.A. Lagum, M.M. Sabugaa, R.D.C. Pecho, H.M. Salman, M.F. Nassar, UV and solar-based photocatalytic degradation of organic pollutants from ceramics industrial wastewater by Fe-doped ZnS nanoparticles, Chemosphere 336 (2023) 139208.

[37] H. Kuruva, V.B. Khavala, B.R. Mishra, K. Murugan, T. Thomas, B.S. Murty, Photocatalytic degradation of multi-organo-sulfur industrial wastewater using TiO_2 produced from modified sulfate process, J. Water Process Eng. 53 (2023) 103805.

[38] G. Zinta, H. AbdElgawad, D. Peshev, J.T. Weedon, W. Van den Ende, I. Nijs, I.A. Janssens, G.T.S. Beemster, H. Asard, Dynamics of metabolic responses to periods of combined heat and drought in *Arabidopsis thaliana* under ambient and elevated atmospheric CO_2, J. Exp. Bot. 69 (2018) 2159–2170.

[39] H. AbdElgawad, A.M. Saleh, S. Al Jaouni, S. Selim, M.O. Hassan, M.A.M. Wadaan, A.M. Shuikan, H.S. Mohamed, W.N. Hozzein, Utilization of actinobacteria to enhance the production and quality of date palm (*Phoenix dactylifera* L.) fruits in a semi-arid environment, Sci. Total. Environ. 665 (2019) 690–697.

[40] S.M. Hamed, S.H. Hassan, S. Selim, M.A.M. Wadaan, M. Mohany, W.N. Hozzein, H. AbdElgawad, Differential responses of two cyanobacterial species to *R*-metalaxyl toxicity: Growth, photosynthesis and antioxidant analyses, Environ. Pollut. 258 (2020) 113681.

[41] W. Abu El-Soud, M.M. Hegab, H. AbdElgawad, G. Zinta, H. Asard, Ability of ellagic acid to alleviate osmotic stress on chickpea seedlings, Plant. Physiol. Bioch. 71 (2013) 173–183.

[42] L. Versieren, S. Evers, H. AbdElgawad, H. Asard, E. Smolders, Mixture toxicity of copper, cadmium, and zinc to barley seedlings is not explained by antioxidant and oxidative stress biomarkers, Environ. Toxicol. Chem. 36 (2017) 220–230.

[43] A. de Sousa, A.M. Saleh, T.H. Habeeb, Y.M. Hassan, R. Zrieq, M.A.M. Wadaan, W.N. Hozzein, S. Selim, M. Matos, H. AbdElgawad, Silicon dioxide nanoparticles ameliorate the phytotoxic hazards of aluminum in maize grown on acidic soil, Sci. Total Environ. 693 (2019) 133636.

[44] P.M. MacFarlane, P.B. Frappell, T. Haase, Respiratory characteristics of the tammar wallaby pouch young and functional limitations in a newborn with skin gas exchange, J. Comp. Physiol. B 191 (2021) 995–1006.

[45] M.M.Y. Madany, W.A. Obaid, W. Hozien, H. AbdElgawad, B.A. Hamed, A.M. Saleh, Salicylic acid confers resistance against broomrape in tomato through modulation of C and N metabolism, Plant. Physiol. Bioch. 147 (2020) 322–335.

[46] A. Norouzi, A. Nezamzadeh-Ejhieh, α-Fe_3O_4/Cu_2O heterostructure: Brief characterization and kinetic aspect of degradation of methylene blue, Physica B 599 (2020) 412422.

[47] I. Ahmad, S.M. Shah, M.N. Zafar, M.N. Ashiq, W. Tang, U. Jabeen, Synthesis, characterization and charge transport properties of Pr-Ni Co-doped $SrFe_2O_4$ spinel for high frequency devices applications, Ceram. Int. 47 (2021) 3760–3771.

[48] S. Ghattavi, A. Nezamzadeh-Ejhieh, A double-Z-scheme ZnO/AgI/WO photocatalyst with high visible light activity: Experimental design and mechanism pathway in the degradation of methylene blue, J. Mol. Liq. 322 (2021) 114563.

[49] M.A. Rafiq, M.A. Khan, M. Asghar, S.Z. Ilyas, I. Shakir, M. Shahid, M.F. Warsi, Influence of Co^{2+} on structural and electromagnetic properties of Mg-Zn nanocrystals synthesized via co-precipitation route, Ceram Int 41 (2015) 10501–10505.

[50] R.S. Yadav, J. Havlica, J. Masilko, L. Kalina, J. Wasserbauer, M. Hajdúchová, V. Enev, I. Kuritka, Z. Kozáková, Cation Migration-induced crystal phase transformation in copper ferrite nanoparticles and their magnetic property, J. Supercond. Nov. Magn. 29 (2016) 759–769.

[51] L. Slavov, M.V. Abrashev, T. Merodiiska, C. Gelev, R.E. Vandenberghe, I. Markova-Deneva, I. Nedkov, Raman spectroscopy investigation of magnetite nanoparticles in ferrofluids, J. Magn. Magn. Mater. 322 (2010) 1904–1911.

[52] T. Ge, Z.K. Jiang, L. Shen, J. Li, Z.Q. Lu, Y.C. Zhang, F. Wang, Synthesis and application of Fe_3O_4/$FeWO_4$ composite as an efficient and magnetically recoverable visible light-driven photocatalyst for the reduction of Cr(VI), Sep. Purif. Technol. 263 (2021) 118401.

[53] H. Derikvandi, A. Nezamzadeh-Ejhieh, Increased photocatalytic activity of NiO and ZnO in photodegradation of a model drug aqueous solution: Effect of coupling, supporting, particles size and calcination temperature, J. Hazard. Mater. 321 (2017) 629–638.

[54] S. Ghattavi, A. Nezamzadeh-Ejhieh, A brief study on the boosted photocatalytic activity of AgI/WO_4/ZnO in the degradation of methylene blue under visible light irradiation, Desalin. Water. Treat. 166 (2019) 92–104.

[55] S. Vahabirad, A. Nezamzadeh-Ejhieh, Evaluation of the photodegradation activity of bismuth oxoiodide/bismuth sub-carbonate nanocatalyst: Experimental design and the mechanism study, Ecotoxicol. Environ. Saf. 263 (2023) 115254.

[56] Q.N. Meng, J.N. Cui, Y.F. Tang, Z.H. Han, K. Zhao, G.J. Zhang, Q. Diao, Solvothermal synthesis of dual-porous CeO_2-ZnO composite and its enhanced acetone sensing performance, Ceram Int 45 (2019) 4103–4107.

[57] M. Wagstaffe, H. Hussain, M.J. Acres, R. Jones, K.L. Syres, A.G. Thomas, Structure and Reactivity of a model oxide supported silver nanocluster catalyst studied by near ambient pressure X-ray photoelectron spectroscopy, J. Phys. Chem. C 121 (2017) 21383–21389.

[58] Z. Amani-Beni, A. Nezamzadeh-Ejhieh, A novel non-enzymatic glucose sensor based on the modification of carbon paste electrode with CuO nanoflower: Designing the experiments by response surface methodology (RSM), J. Colloid Interf. Sci. 504 (2017) 186–196.

[59] M. Nosuhi, A. Nezamzadeh-Ejhieh, High catalytic activity of Fe(II)-clinoptilolite nanoparticales for indirect voltammetric determination of dichromate: Experimental design by response surface methodology (RSM), Electrochim. Acta 223 (2017) 47–62.

[60] Z. Amani-Beni, A. Nezamzadeh-Ejhieh, NiO nanoparticles modified carbon paste electrode as a novel sulfasalazine sensor, Anal Chim. Acta 1031 (2018) 47–59.

[61] F. Zhang, Y. Shen, M. Shao, Y.C. Zhang, B. Zheng, J.S. Wu, W.N. Zhang, A.P. Zhu, F.W. Huo, S. Li, $SnSe_2$ Nanoparticles chemically embedded in a carbon shell for high-rate sodium-ion storage, ACS Appl. Mater. Interfaces 12 (2020) 2346–2353.

[62] Y. Zhang, L. Hu, Y.C. Zhang, X.Z. Wang, H.G. Wang, Snowflake-Like Cu_2S/MoS_2/Pt heterostructure with near infrared photothermal-enhanced electrocatalytic and photoelectrocatalytic hydrogen production, Appl. Catal. B 315 (2022) 121540.

[63] N. Sharma, V. Sharma, R. Vyas, M. Kumari, A. Kaushal, R. Gupta, S.K. Sharma, K. Sachdev, A new sustainable green protocol for production of reduced graphene oxide and its gas sensing properties, J. Sci.-Adv. Mater. Dev. 4 (2019) 473–482.

[64] S.A. Mirsalari, A. Nezamzadeh-Ejhieh, Focus on the photocatalytic pathway of the CdS-AgBr nano-catalyst by using the scavenging agents, Sep. Purif. Technol. 250 (2020) 117235.

[65] S. Senobari, A. Nezamzadeh-Ejhieh, A comprehensive study on the enhanced photocatalytic activity of CuO-NiO nanoparticles: Designing the experiments, J. Mol. Liq. 261 (2018) 208–217.

[66] Z. Wang, D. Wang, F. Deng, X. Liu, X. Li, X. Luo, Y. Peng, J. Zhang, J. Zou, L. Ding, L. Zhang, Ag quantum dots decorated ultrathin g-C_3N_4 nanosheets for boosting degradation of pharmaceutical contaminants: Insight from interfacial electric field induced by local surface plasma resonance, Chem. Eng. J. 463 (2023)

142313.
[67] F. Deng, J. Peng, X. Li, X. Luo, P. Ganguly, S.C. Pillai, B. Ren, L. Ding, D.D. Dionysiou, Metal sulfide-based Z-scheme heterojunctions in photocatalytic removal of contaminants, H_2 evolution and CO_2 reduction: Current status and future perspectives, J. Clean. Prod. 416 (2023) 137957.
[68] R. He, Z. Wang, F. Deng, X. Li, Y. Peng, Y. Deng, J. Zou, X. Luo, X. Liu, Tunable Bi-bridge S-scheme Bi_2S_3/BiOBr heterojunction with oxygen vacancy and SPR effect for efficient photocatalytic reduction of Cr(VI) and industrial electroplating wastewater treatment, Sep. Purif. Technol. 311 (2023) 123176.
[69] C. Lai, D.S. Ma, H. Yi, M.M. Zhang, F.H. Xu, X.Q. Huo, H.Y. Ye, L. Li, L. Yang, L. Tang, M. Yan, Functional partition of Fe and Ti co-doped g-C3N4 for photo-Fenton degradation of oxytetracycline: Performance, mechanism, and DFT study, Sep. Purif. Technol. 306 (2023) 122546.
[70] S. Ghattavi, A. Nezamzadeh-Ejhieh, A visible light driven AgBr/g-C_3N_4 photocatalyst composite in methyl orange photodegradation: Focus on photoluminescence, mole ratio, synthesis method of g-C_3N_4 and scavengers, Compos. B Eng. 183 (2020) 107712.
[71] M. Farsi, A. Nezamzadeh-Ejhieh, A Z-scheme cobalt(II) oxide-silver tungstate nano photocatalyst: Experimental design and mechanism study for the degradation of methylene blue, Surf. Interfaces 32 (2022) 102148.